Distortion-free "inside-out" imaging for rapid diagnostics of rechargeable Li-ion cells

Konstantin Romanenko [a] and Alexej Jerschow * [a]

Department of Chemistry, New York University, 100 Washington Square East, New York, NY 10003.

E-mail: alexej.jerschow@nyu.edu

Author contributions: K.R. and A.J. designed research; K.R. performed research and analyzed data; and K.R. and A.J. wrote the paper.

inside-out MRI|SPRITE|battery diagnostics|Li-ion batteries

Abstract

The potential safety risks associated with modern high energy-dense rechargeable batteries highlight the need for advanced battery screening technologies. A common rechargeable cell exposed to a uniform magnetic field creates a pattern of magnetic field perturbation due to the inherent magnetism of the battery materials and components. This effect depends on the battery design, state of charge, accumulated mechanical defects and history of the cell. The visualization of this induced magnetic field by means of MRI allows rapid non-invasive testing of commercial-type batteries. Here we introduce a quantitative distortion-free approach for battery diagnostics based on magnetic field mapping with Single Point Ramped Imaging with T_1 enhancement (SPRITE). This method avoids image perturbations arising from background magnetic field gradients and eddy currents. The method is demonstrated on commercial Li-ion pouch cells and iPhone-5 batteries. SPRITE is particularly suitable for cell diagnostics due to its robustness to artefacts in regions with large local field variations. The method is demonstrated to show superior image quality and the extracted magnetic field maps are shown to be sensitive to defects and the state of charge distribution in batteries with strongly magnetic components.

Significance

Rechargeable batteries can pose severe safety risks due to their flammable components in combination with high energy density. These challenges motivate the development of new advanced battery screening techniques capable of rapid battery assessment. MRI, a broadly accepted method in the health care industry, has been adapted for materials chemistry and energy storage research. A quantitative MRI approach based on 3D phase encoding bypasses the hurdles associated with strongly magnetic components that are common in modern batteries (e.g. iPhone models). The reported technology is virtually distortion-free and shows a high sensitivity to mechanical defects and the chemical state of the electrodes. This approach may enable industrial quality control applications with a high temporal resolution and may aid in battery development and monitoring.

\body

The wide use of portable electronics and rapidly expanding market for electric vehicles have driven the demand for high capacity and safe rechargeable batteries. Challenges arise due to the presence of flammable materials in batteries and power banks and their high energy densities. Noninvasive means for battery diagnostics are being developed in efforts to predict and characterize battery failure modes (1-4). Magnetic resonance imaging (MRI) is an established powerful tool for studying chemical, biological and solid-state phenomena (5-8). NMR spectroscopy and MRI have provided the ability to investigate electrochemical cells under *in situ* or *operando* modes and have thus provided important information on underlying physical and mechanistic processes (9-16). These techniques could not, until recently, be used to study commercial cells due to the conductive casings and small distances between electrodes, which hamper radiofrequency (RF) penetration. As a result, such studies were typically limited to the use of model devices.

Recently, an "inside-out" MRI (ioMRI) approach was introduced that allowed to overcome the limitations imposed by RF penetration through conductive regions (1). The distribution of the magnetic field (MF) created by a cell depends on the magnetic susceptibility and morphology of its constituents. For example, the source of a strong induced magnetization in rechargeable lithium-ion batteries is often a lithium intercalation compound. The value of the magnetic susceptibility changes as a function of the amount of inserted lithium. For this reason, it has been shown that Li-intercalation and its state of charge (SOC) could be assessed in cells non-destructively and rapidly by ioMRI. Furthermore, it was demonstrated that defects could be diagnosed in this fashion as well.

Faulty cells can exhibit unique MF features characteristic of their defects. Industrial-scale applications of such battery diagnostics should ideally employ rapid MRI methods (e.g. Fast Spin Echo - FSE, Fast Low Angle Shot - FLASH, Echo Planar Imaging - EPI) in combination with compressed sensing and parallel imaging (17). These techniques rely on either long evolution times and echo trains, frequency encoding, or slice selective RF pulses. Conductive and paramagnetic components within the imaged volume result in artefacts from susceptibility contrast and eddy currents induced by radio frequency (RF) and gradient pulses (18-20). Background MF gradients (transient or permanent) have adverse effects on image quality, particularly in the case of gradient echo (GRE) based MRI, e.g. FLASH. Several complications arise: (a) Signals in the vicinity of such features can decay rapidly due to destructive interferences within the voxels, and (b) strong background gradients lead to image misregistration.

Both these problems can be addressed with fully phase-encoded 3D acquisition, which eliminates signal evolution. Thus, compromising effects of any internal field gradients during image acquisition are avoided. Single point ramped imaging with T_1 enhancement, SPRITE (21-24), is a pure phase encoding technique, successfully employed in a range of challenging studies including solid-state and turbulent flow imaging (14, 25-29). Here, we implement a SPRITE-based MF mapping technique for the purposes of performing ioMRI on rechargeable battery cells. It is found that the SPRITE-ioMRI approach provides accurate artefact-free MF visualization, especially in regions with strong local magnetism. This approach is particularly important as strongly magnetic materials are often incorporated into many commercial cells. The SPRITE-ioMRI approach is shown here to represent a reliable diagnostic tool for commercial cells, including, for example, iPhone batteries. It is demonstrated that SOC distributions can be determined with this method, and unique cell features and defects could be located.

Concepts of the SPRITE-ioMRI

The phenomenon of magnetic resonance (MR) is based on the Zeeman interaction (5) and the use of static and oscillating pulsed MF's to manipulate transitions between nuclear spin energy levels. An extension of this idea, MRI, uses pulsed MF gradients to create a spatial variation of resonance frequencies. Conceptually, one may define a reciprocal *k*-space, F($\boldsymbol{k}$), of spatial frequencies (30, 31), which represents the grid of raw data acquisition points, according to

$$F(\boldsymbol{k}) = \Sigma A(\boldsymbol{r}) \exp(-\boldsymbol{i}2\pi\, \boldsymbol{k}\, \boldsymbol{r}). \qquad (1)$$

An image, A($\boldsymbol{r}$), can be obtained via a Fourier transformation of experimentally measured F($\boldsymbol{k}$). A MR signal is acquired for discrete values of the vector $\boldsymbol{k} = \gamma\, \boldsymbol{g}\, t\, (2\pi)^{-1}$, where γ is the nuclear gyromagnetic ratio, $\boldsymbol{g}$ is the MF gradient vector and t is time. *K*-space sampling may be performed by varying either time (frequency encoding) or the gradient magnitude (phase encoding). The concept of single point MRI relies exclusively on phase encoding. The main building block of the 3D centric-scan SPRITE experiment is shown in Fig. 1 *A*. Key parameters of the pulse sequence are the applied MF gradient $\boldsymbol{g}(g^X, g^Y, g^Z)$, the gradient ramp time T_{GR}, the gradient stabilization time T_{GS}, the RF pulse flip angle α and pulse duration P_α, the phase encoding time T_P, the number of complex data points sampled per gradient step *TD*, the repetition period T_R, the pulse train length N_{TR}, the number of interleaves N_{int}, and the recovery delay between the pulse trains T_0.

The sequence starts at the *k*-space origin ($\boldsymbol{g} = 0$) with a non-selective RF excitation followed by a period of free precession (T_P) and the acquisition of a single sample of the free induction decay (FID). In the next loop, the imaging gradient $\boldsymbol{g}$ is ramped to the next value over a period of time T_{GR} and is allowed to stabilize during T_{GS}. The following RF excitation, free precession (phase encoding) and single point acquisition events take place in the presence of this gradient. MR signals measured for a full range of discrete $\boldsymbol{g}$ values represent a purely phase encoded *k*-space. Although it is possible to execute the SPRITE loop continuously until all *k*-space data are acquired, the gradient and RF hardware duty cycles can approach levels that cannot be sustained reliably by the equipment. To prevent overheating, it is recommended to perform an interleaved *k*-space sampling. The whole *k*-space can be divided into N_{int} interleaves. One interleaf is sampled with a train of N_{TR} "P_α - T_P - ACQ" blocks. T_0 is set to $\approx 5\ T_1$ (spin-lattice relaxation time constant). The interleaved acquisition allows for control over the temperature inside the gradient coil system and RF circuit, and improves the image resolution (23, 24).

A fundamental property of Fourier transformation suggests that $F(\boldsymbol{k} = 0)$ is a measure of total spin density (Eq.1). Thus, commencing *k*-space sampling at $\boldsymbol{k} = 0$ is crucial for the quantitative measurement of the longitudinal magnetization and optimal SNR (22). Repetitive RF pulses result in a temporal evolution of the longitudinal magnetization and modulate the *k*-space envelope. As a result, image blurring occurs. The image resolution depends on T_1 and can be optimized by adjusting α (22-25).

Assigning gradient values to locations on the Cartesian grid is a robust and convenient sampling approach (23, 24). In this case, the image reconstruction consists of two simple steps: (a) re-ordering of the raw data into a 3D complex array based on predetermined gradient tables (g_k^X, g_k^Y, g_k^Z), and (b) a fast discrete Fourier transformation. As an example, sectoral interleaves employed in this work are shown in Fig. 1 *B*. The *k*-space matrix $N^X \times N^Y \times N^Z$ is sampled plane-by-plane along *Z*. The in-plane trajectories (*X*-*Y*) are unwinding spirals confined within eight sectors ($N_{int} = 8$). One of the advantages of the sectoral sampling scheme is that the blurring is distributed uniformly in the *X*-*Y* plane (11). Note that P_α should be sufficiently short to excite the maximum sample bandwidth $\gamma G^{X,Y,Z} L^{X,Y,Z} (2\pi)^{-1}$, $G^{X,Y,Z}$ is the maximum gradient magnitude along the principal gradient axes, and $L_{X,Y,Z}$ are the sample dimensions along *X, Y* and *Z*. Typically, α is a few degrees and P_α is a few microseconds long.

The shortest T_R is limited by the hardware performance and safety requirements specific to RF and gradient duty cycles. The realistic range of T_R values is from 0.5 to 2 ms. T_P is the constant time

interval between the end of RF pulse and the end of the signal acquisition. The range of T_P's from 10 to 100 μs is achievable depending on the RF probe "dead" time.

The image field of view (FOV) is

$$FOV^{X,Y,Z} = 2\pi\, N^{X,Y,Z} \left(\gamma\, G^{X,Y,Z}\, T_P \right)^{-1}. \qquad (2)$$

The phase of the local transverse magnetization accumulated due to free precession over the time T_P is

$$\varphi(\boldsymbol{R}) = \gamma\, \Delta B_0(\boldsymbol{R})\, T_P, \qquad (3)$$

where $\Delta B_0(\boldsymbol{R}) = B(\boldsymbol{R}) - B_0$ is the local perturbation of static magnetic field associated with the susceptibility contrast. The complex MR signal measured at location $\boldsymbol{R}$ at time T_P after the excitation pulse is described by the product of oscillating and attenuation terms,

$$S(\boldsymbol{R}, T_P) = I_Z \sin(\alpha) \exp(\boldsymbol{i}\, 2\pi\, \nu(\boldsymbol{R})\, T_P) \exp(-T_P / T_2^*), \qquad (4)$$

where I_Z is the equilibrium nuclear magnetization, $\nu(\boldsymbol{R}) = \gamma\, \Delta B_0(\boldsymbol{R})(2\pi)^{-1}$ is the local Larmor frequency offset. The time constant, T_2^*, describing the rate of magnetization attenuation attributable to the intrinsic NMR linewidth ($\Delta\nu_{1/2}$), is determined via spin-spin relaxation rate ($1/T_2$) and magnetic field inhomogeneity (ΔB) across a voxel according to

$$T_2^{*-1} = T_2^{-1} + \gamma\, \Delta B\, (2\pi)^{-1}. \qquad (5)$$

The signal phase, $\varphi = \arctan\{\mathrm{Im}(S) / \mathrm{Re}(S)\}$, measured as a function of T_P (Eq. 3) gives

$$\nu(\boldsymbol{R}) = (2\pi)^{-1}\, d\varphi / dT_P. \qquad (6)$$

The ambiguity arises from potential phase wrapping (by multiples of 2π). Unwrapped phases can be obtained by established procedures (32). The sensitivity of the method depends on the range and the number of phase encoding intervals.

Although separate SPRITE scans using multiple T_P values can provide superior sensitivity, the MF map can be reconstructed from just one SPRITE scan ($N_{TP} = 1$). Acquiring several phase-

encoded points (*TD*) per RF excitation in a single FID readout allows for a significant improvement in time efficiency. Another benefit of this approach is a higher accuracy of the measured average phase due to reduced phase dispersion over the shorter delays. Note, since the acquisition occurs in the presence of an applied MF gradient, each point corresponds to a different field-of-view (FOV). For the MF calculation, one therefore needs to scale these FOVs using an established chirp Z-transform algorithm (23).

The 3D MF mapping experiment duration is

$$(N^3 T_R + N_{int} T_0) N_{TP}, \quad (7)$$

where N_{TP} is the number of T_P intervals. Note that SPRITE imaging can be implemented as a 1D, 2D or 3D modality and we provide corresponding experiment durations as a general guideline. A 1D SPRITE profile (N_{1D} = 128, N_{int} = 2, T_R = 1 ms, T_0 = 1 s) consumes approximately 2 s. A 2D sectoral experiment (N_{2D} = 64, N_{int} = 8, T_R = 1 ms, T_0 = 1 s) could be acquired within 12 seconds. A 3D sectoral acquisition (N_{3D} = 64, N_{int} = 64×8, T_R = 1 ms, T_0 = 1 s) consumes 13 minutes. 3D SPRITE experiments can be substantially accelerated, depending on T_0 and T_R (hardware limitations), and the choice of *k*-space sampling strategy. For comparison, a FLASH-based MF map (128×128×128) consumes 10 minutes with four echo times (*TE*).

Regardless of the MRI technique, the signal intensity is directly proportional to the voxel volume, and the practical MRI resolution is largely limited by the signal-to-noise ratio (SNR). MF can be inhomogeneous at the macroscopic level (larger than a voxel) or the microscopic (sub-voxel) scale. In the latter case, small structures can be identified due to the partial volume effects even with relatively coarse resolution (1 mm) of SPRITE acquisition.

The magnetic susceptibility phenomenon and ioMRI measurements are outlined for a cylindrical paramagnetic sample ($MnCl_2$ solution in a capillary) with the T_2*-weighted density maps and corresponding patterns of MF perturbations, Fig. S1. SPRITE provides excellent accuracy: + 4.5 ppm near the bottom and top of the capillary is in good agreement with the expected value (+ 4.59 ppm) calculated based on the molar susceptibility of $MnCl_2$ ($+14350 \cdot 10^{-6}$ cm^3 mol^{-1}).

The following points highlight some benefits of the SPRITE design:

(a) Pure phase encoding is immune to image artefacts arising from susceptibility contrast and chemical shift.

(b) The short phase encoding period (< 0.1 ms) prevents a significant attenuation of transverse magnetization due to spin-spin relaxation, dephasing and diffusion in background gradients, and is a prerequisite quantitative and time-efficient broad line MRI applications.

(c) The SPRITE concept provides flexibility in *k*-space sampling strategies. This flexibility is important for the optimization of image resolution, contrast, measurement time, and gradient and RF duty cycles.

(d) Commencing *k*-space sampling at $\boldsymbol{k} = 0$ is crucial for the quantitative measurement of the longitudinal magnetization and optimal SNR.

(e) After each signal acquisition, the "leftover" transverse magnetization is effectively spoilt by the gradients applied over following T_{GR} and T_{GS} intervals.

(f) Acoustic noise induced by gradient switching is insignificant due to low amplitude gradient increments.

(g) There are no stringent requirements on the gradient system performance as accurate phase encoding is unaffected by the gradient pulse shape in the switching periods.

Results and discussion

In the approach described previously by Ilott et al. (1), the cell is placed inside the dedicated battery holder, and a series of FLASH images is acquired with different echo times. Note that the ^{1}H MRI signal originates from the aqueous solution confined inside two detection volumes of the holder and not from the battery itself (thus the term "inside-out" was introduced). Figure 1 *C* shows the arrangement of the cell, the detection volumes and the directions of the polarizing (B_0) and RF (B_1) magnetic fields. The orientation of the cell was selected to maximize B_1 homogeneity (9-11). The magnetic field maps were produced from fitting the signal phase as a function of *TE*, in combination with a suitable phase unwrapping algorithm.

Below, we compare the results of FLASH and SPRITE-based ioMRI tests of iPhone-5 batteries. The cells contain strongly paramagnetic as well as some ferromagnetic components. This situation could represent a "no go zone" for conventional MRI methods employing frequency encoding and slice-selective pulses. A 3D FLASH density image (T_2*- weighted) of the holder containing the iPhone-5 battery illustrates this point (Fig. 2 *A*). The positions and orientations of the 3D image slices with respect to the battery are indicated in Fig. 1 *C* with red {*x*-*z*} and blue {*y*-*z*} dashed lines. Since the battery's length exceeded the extent of the uniform spot of the MiniWB57 RF resonator, the upper and lower halves of the battery were scanned separately, and two images were combined.

The image regions near the center and the leads (bottom) of the cell were severely affected by MF inhomogeneity induced by the spatial variation in susceptibility. The corrupted domains occupied a significant part of the detection volume (Fig. 2 *A*). The metal components present in the battery gave rise to two types of MRI artefacts: (a) complete loss of signal due to rapid dephasing of

transverse magnetization (short T_2*) and (b) geometric distortions in the form of high frequency ripples. A theoretical description of signal misregistration in gradient-echo MRI is provided by Reichenbach et al (33).

The low intensity voxels (SNR < 1) contained short-lived magnetization components with T_2* < 0.1 ms (Eq. 3). The spread of Larmor frequencies $\gamma \Delta B (2\pi)^{-1} > 3$ kHz on the length scale of voxel (≈ 0.4 mm) resulted in total dephasing of the transverse magnetization over the FLASH *TE* (2.5 ms). Significant signal loss can also be associated with the shifting of the gradient echo outside the acquisition window.

The source of the geometric distortions is the "contamination" of the applied frequency encoding gradient by "unaccounted for" background gradients. By design, frequency encoding is the detection of transverse magnetization in the presence of a constant and uniform MF gradient. Any arbitrary gradients added to this applied gradient will produce unwanted frequency shifts in *k*-space thus assigning spins to false locations and alter true intensity values.

The longitudinal slices through the FLASH-derived 3D MF map are shown in Fig. 2 *B*. The binary mask applied to this map was calculated from the 3D FLASH reference image of the empty holder. The mask shows all voxels containing H_2O (i.e. space inside the holder excluding the battery compartment) including the ones with extremely short T_2*. Phase data and local accuracy of the calculated MF field are compromised the most in these domains with the strongest background gradients. To further demonstrate the limited applicability of FLASH, Figure 2 *C* shows only voxels where the signal magnitude is above 20% of the overall density image maximum. Although the local SNR could be improved by signal averaging (at the expense of experiment time) the misregistration artefacts will remain. They can be mitigated to some degree by increasing the sampling bandwidth and frequency encoding gradient magnitude.

The SPRITE density images illustrate their robustness against distortions (Fig. 3 *A*). With T_P = 0.12 ms, a T_2* - weighting effect was seen near the center. The SPRITE MF map, Fig. 3 *B*, shows well-defined patterns in the "difficult" regions that are not accessible to FLASH (Fig. 2 *C*). Here, SPRITE detected a frequency range that was almost three times larger than that what was seen by FLASH.

The "8" - shaped feature near the center of FOV can be attributed to slightly ferromagnetic material inside the cell. Upon disassembly, this material was found to be a part of a Ni-plated tab. The extent of the arrangement is shown in Fig. 3 *C*. Above the tip of the metal strip, the MF perturbation exceeded +20 ppm, while below the tip, MF was below -20 ppm. At 9.4 T, a MF variation of 40 ppm over a 5 mm distance is equivalent to a MF gradient of 75 mT m^{-1}. The temporal

evolution of the SPRITE signal phase is illustrated for two representative locations exhibiting positive and negative frequency shifts in Fig. S2.

Figure 4 shows the MF maps of two damaged iPhone-5 batteries. Figure 4 *A* shows the effect of a 4 mm diameter hole punched in the center of the lower half of the battery, as indicated on the right. The magnetic tab of this battery was cut and removed from that location. An effect of a 16 mm diameter hole is demonstrated in Fig. 4 *B*. The ferromagnetic metal strip was cut in half and the upper half was extracted. The image shows a striking MF pattern associated with the defect and the leads. Note, that the "8"-shaped MF pattern in Fig. 3 *B*, observed near the center of the intact battery disappeared. Instead, the high MF field "cloud" emerged at the tip of the remaining half of the metal strip. Similar patterns were seen for the two leads at the bottom.

Next, we demonstrate the sensitivity of the method to certain defect features. Figure 5 shows photographs of an intact PowerStream (PS) cell (*A*) and the same cell after introducing mechanical damage (*B*). The defect at the center of the battery was produced by impacts with a metal cylinder of 10 mm diameter. Three impacts were applied to the same spot (0.79 cm^2) with the energy of 1.2 J per impact and led to a highly visible imprint of a depth of approximately 0.5 mm. A bulge was formed on the opposite side of the battery. The cell voltage, however, was not affected by this damage.

MF maps of the intact (Fig. 5 *C* - FLASH, Fig. 5 *E* - SPRITE) and damaged (Fig. 5 *D* - FLASH, Fig. 5 *F* - SPRITE) PS cells showed noticeable differences. The position and orientation of the {*x*-*z*} slice with respect to the cell are indicated in Fig. 1 *C*. The MF perturbation by the intact cell was symmetrical and approached +25 ppm above and below (outside the FOV) the battery. The damaged battery (Fig. 5 *D* and *F*) exhibited noticeable asymmetry of MF. These changes are consistent with simulations of MF perturbations by "impressions" and "bulges" on the surface of paramagnetic objects (13).

MF perturbations observed by FLASH and SPRITE were different in magnitude and morphology. According to the SPRITE measurements (Fig. 5 *E* and *F*) the MF increased by up to 6 ppm near the region of impact, while on the opposite side of the cell the field decreased by up to 2 ppm. Importantly, the FLASH MF values were found within a much narrower range of frequencies (from -4 to +8 ppm) as compared to the SPRITE data (from -10 to +25 ppm). Near the region of impact, the maximum change in MF detectable by FLASH was close to 1 ppm. The FLASH images were also affected by ripple-like misregistration artefacts near the battery.

The discrepancy between SPRITE and FLASH based MF measurements is partially attributed to the different extent of T_2* weighting, originating from a distribution of Larmor frequencies within

the voxels. The most accurate MF measurement can be performed by collecting phase data immediately after the RF excitation pulse. This is the major technical limitation for all conventional MRI methods employing long evolution times. The high frequency components are effectively filtered out by long *TE's* in the FLASH method. In voxels exhibiting a linewidth of $\gamma \Delta B (2\pi)^{-1}$, such that $TE >> 2\pi (\gamma \Delta B)^{-1}$, the FLASH signal would be completely suppressed. Furthermore, once significant intra-voxel averaging occurs, the field map derived from the overall phase measurement seizes to be accurate even before the signals decay. In addition, the high frequencies are suppressed by echo shifting and assigned to wrong locations as a result of misregistration (33). By contrast, SPRITE suffers only from a minimal T_2*-weighting since its MF sensitizing period is much shorter (0.1 ms). Since SPRITE imaging is distortion-free, the main limitation for SPRITE-based ioMRI applications arises from T_2* times, short compared to T_P. The sensitivity limit can be established as $T_P \approx 5T_2$*. Assuming $T_P < 50$ μs, the detectable range of frequencies $\Delta\nu_{1/2} = (\pi T_2^*)^{-1}$ is ≈ 30 kHz, i.e. 75 ppm in 9.4 T. A background gradient generating this linewidth over a 1 mm voxel (700 mT m^{-1}) is much greater than gradients produced by typical MRI systems (20–100 mT m^{-1}).

A relationship between SOC and susceptibility provides a mechanism of ioMRI contrast suitable for accurate battery diagnostics. In order to remove MF components independent of SOC, the fully charged iPhone-5 battery served as a reference sample. The reference MF map was subtracted from maps of the battery at different SOC. The histograms of MF perturbation variation ($\delta\Delta B_0$) due to SOC are shown in Figure 6. This experiment demonstrates that despite the presence of large field distortions in these cells, the subtler changes in SOC distributions can easily be detected with the SPRITE approach. A stronger SOC effect observed in PS batteries (Fig. S3) was attributed to the overall higher content of magnetic elements, in particular Co. Charging the battery (500 mA h) resulted in up to a 4 ppm change in the local MF.

The cathode chemistry and composition determine the MF variations associated with SOC. This consideration is in line with electron-dispersive X-ray spectroscopy (EDX) analysis, which showed that the cathode of the iPhone-5 model had 13.6 Wt% Co, 13.2 Wt% Ni and 7.8 Wt% Mn (Fig. S4), while the PS batteries contained Co (29 Wt%), Ni (6.8 Wt%), and Mn (4.8 Wt%) (Fig. S5).

In summary, paramagnetic electrodes and ferromagnetic metal components are common ingredients of the battery manufacturing process. We demonstrated a distortion-free ioMRI battery diagnostics based on centric-scan SPRITE technique. Pure phase encoding (3D) with short phase encoding times is a preferred approach in applications to systems exhibiting broad NMR lines. The

major benefit of SPRITE is the ability to accurately visualize the magnetic field around devices containing strongly magnetic components. In addition to the superior image quality, a high temporal resolution can be achieved, which is suitable for in situ battery characterization and commercial quality control applications. The method is highly sensitive to mechanical defects and can distinguish fine changes in the electrode's chemical states and composition. Examples of practical relevance of the presented work are the Samsung Galaxy Note 7 battery failures (overheating and catching fire) highlighted in mass media in 2016. These were attributed in part to mechanical defects arising from errors in design and manufacturing.

Materials and Methods

Magnetic resonance imaging

MRI experiments were carried out using a Bruker Avance instrument equipped with a 9.4 T vertical 89 mm bore magnet (400.11 MHz ^{1}H frequency), a Mini0.75 water-cooled triaxial gradient system driven by GREAT (1/40) amplifiers each providing 0.45 T m^{-1} maximum gradient. The RF excitation and ^{1}H MRI signal detection were achieved with a 40 mm i.d. "bird cage" resonator (MiniWB57 probe). The 3D SPRITE pulse sequence was programmed under the Bruker ParaVision5.2 environment. The following SPRITE parameters were used: P_α, 4 μs; α, π/40; T_{GR}, 1 ms; T_{GS}, 0.9 ms; $T_R \approx 2$ ms; T_0, 2 s; TD, 16; dw, 5 μs, T_P varied in the range from 70 to 360 μs. The SPRITE gradient magnitudes were determined based on T_P*'s* and a fixed FOV as $2\pi N (\gamma\ FOV\ T_P)^{-1}$ (Eq. 1). 3D centric-scan SPRITE experiments ($N_{3D} = 37$, $N_{int} = 37\times4$, $T_R = 2$ ms, $T_0 = 2$ s) and ($N_{3D} = 64$, $N_{int} = 64\times8$, $T_R = 2$ ms, $T_0 = 2$ s) consumed 6.6 and 25 minutes, respectively, with one signal average. The acquired *k*-space matrix 37 × 37 × 37 was zero-padded to 64 × 64 × 64. The rapid MF mapping approach based on one SPRITE scan used eight FID points per gradient step (DW = 5 μs) giving rise to eight complex 3D phase images. The FOV of each image was scaled using a chirp *Z*-transform algorithm (24). The corresponding range of phase encoding intervals was from 112 – 147 μs. Image reconstruction and data processing were performed using Matlab (R2018b, The MathWorks, Inc.). The 3D phase maps were calculated from real and imaginary components of the complex centric-scan SPRITE images. Local ΔB_0 values were calculated by voxel-by-voxel linear regression of the temporal phase evolution (Eq. 5). The MF map of the holder with the empty battery compartment was used as a reference image.

The FLASH protocol was a standard 3D sequence with linearly ordered phase encoding (Bruker ParaVision 5.2, echo time mode "Short_TE"). Acquisition of one isotropic image 128 × 128 × 128 consumed approximately 2.5 minutes. MF maps were reconstructed from four FLASH images acquired with gradient echo times in the range from 2.45 to 2.8 ms.

Samples

The phantom was a 2.3 mm i.d. 3 mm o.d. capillary containing 0.042 ml of aqueous solution of $MnCl_2$ (0.32 M). The capillary was placed inside a 35 mm o.d. plastic bottle filled with $CuSO_4$ solution (6 mM, T_1 = 180 ms).

Lithium polymer batteries (PowerStream Technology; model PPGEB-NM053040; dimensions 40 x 30 x 5 mm; charge state 3.7 V), and iPhone-5 batteries (dimensions 90 x 30 x 3 mm; charge state 3.77 V) were examined.

One PS cell underwent a controlled damage by dropping a metal rod with 10 mm diameter and 40 cm length from a height of 40 cm. The energy of impact was 1.2 J. The produced defect did not noticeably affect the battery voltage.

iPhone batteries were pierced with a cylindrical metal pole and holes of 4 and 16 mm diameters were created. The MRI experiments were conducted 12 hours after the damage was produced. Due to discharging through inter-layer short circuiting, the damaged iPhone batteries showed no voltage.

The battery holders were designed in the form of a cylindrical vessel (outer diameter 39 mm) with three compartments (1). These were designed using a QIDI TECH I 3D printer (QIDI Technology, China). Two semi-cylindrical compartments were filled with aqueous $CuSO_4$ solution (6 mM, T_1 = 180 ms) serving as the medium for MF mapping. The central compartment accommodated the battery and was isolated from the other two (Fig. 1 *C*).

Holders designed for PS and iPhone-5 batteries had a 5.8 × 34 × 60 and 4.5 × 32 × 60 mm battery compartment, respectively. The iPhone-5 battery was screened one half at a time since the battery length exceeded the length of RF resonator. The images of the halves were combined to form a complete image.

Energy Dispersive X-ray Spectroscopy Microanalysis (EDX) of the battery electrodes was conducted using a MERLIN (Carl Zeiss) field emission scanning electron microscope (FESEM) with an Oxford Instruments EDX setup.

Acknowledgements

Funding is acknowledged from a US National Science Foundation award CBET 1804723 and a research agreement with Mercedes-Benz Research & Development North America. We thank Mohaddese Mohammadi and Trinanjana Mandal for assistance in the EDX microanalysis of the electrodes.

References

1. Ilott AJ, Mohammadi M, Schauerman CM, Ganter MJ, Jerschow A (2018) Rechargeable lithium-ion cell state of charge and defect detection by in-situ inside-out magnetic resonance imaging. *Nat Comm* 9:1776.

2. Eastwood DS, et al. (2015) Three–dimensional characterization of electrodeposited lithium microstructures using synchrotron X-ray phase contrast imaging. *Chem Commun* 51:266–268.

3. Gallaway JW, et al. (2014) Real-time materials evolution visualized within intact cycling alkaline batteries. *J Mater Chem* A 2: 2757–2764.

4. Hsieh AG, et al. (2015) Electrochemical-acoustic time of flight: in operando correlation of physical dynamics with battery charge and health. *Energy Env Sci* 8:1569–1577.

5. Blümich B (2000) *NMR Imaging of Materials* (Oxford University Press, Oxford).

6. Stapf S, Han S (2006) *NMR Imaging in Chemical Engineering* (Wiley-VCH, Weinheim).

7. Koptyug IV (2012) MRI of mass transport in porous media: Drying and sorption processes. *Prog Nucl Magn Reson Spectrosc* 65:1–65.

8. Romanenko K (2017) MRI studies of plastic crystals. *Ann Rep NMR Spectr* 91:67–114.

9. Chandrasekar S, et al. (2012) Li-7 MRI of Li batteries reveals location of microstructural lithium. *Nat Mater* 11:311–315.

10. Ilott AJ, et al. (2014) Visualizing skin effects in conductors with MRI: (7)Li MRI experiments and calculations. *J Magn Reson* 245:143–149.

11. Romanenko K, Forsyth M, O'Dell LA (2014) New opportunities for quantitative and time efficient 3D MRI of liquid and solid electrochemical cell components: Sectoral Fast Spin Echo and SPRITE. *J Magn Reson* 248:96-104.

12. Chang HJ, et al. (2015) Correlating Microstructural Lithium Metal Growth with Electrolyte Salt Depletion in Lithium Batteries Using 7Li MRI. *J Am Chem Soc* 137:15209–15216.

13. Ilott AJ, Mohammadi M, Chang HJ, Grey CP, Jerschow A (2016) Real-time 3D imaging of microstructure growth in battery cells using indirect MRI. *Proc Natl Acad Sci* 113:10779–10784.

14. Romanenko K, Jin L, Howlett P, Forsyth M (2016) In situ MRI of operating solid-state lithium metal cells based on ionic plastic crystal electrolytes. *Chem Mater* 28:2844–2851.

15. Ilott AJ, Jerschow A (2018) Probing Solid-Electrolyte Interphase (SEI) Growth and Ion Permeability at Undriven Electrolyte–Metal Interfaces Using 7Li NMR. *J Phys Chem C* 122:12598–12604.

16. Niemöller A, Jakes P, Eichel R-A, Granwehr J (2018) EPR Imaging of Metallic Lithium and its Application to Dendrite Localisation in Battery Separators. *Scientific Reports* 8:14331.

17. Bernstein MA, King KF, Zhou XJ (2004) Handbook of MRI Pulse Sequences (Illustrated Ed. Elsevier).

18. Graf H, Steidle G, Martirosian P, Lauer UA, Schick F (2006) Effects on MRI due to altered rf polarization near conductive implants or instruments. *Med Phys* 33:124–127.

19. Lee MJ, et al. (2007) Overcoming artifacts from metallic orthopedic implants at high-field-strength MR imaging and multi-detector CT. *Radiographics* 27:791–803.

20. Graves MJ, Mitchell DG (2013) Body MRI artifacts in clinical practice: a physicist's and radiologist's perspective. *J Magn Reson Imaging* 38:269–287.

21. Balcom BJ, et al. (1996) Single-point ramped imaging with T-1 enhancement (SPRITE). *J Magn Reson A* 123:131–134.

22. Mastikhin IV, Balcom BJ, Prado PJ, Kennedy CB (1999) SPRITE MRI with prepared magnetization and centric k-space sampling. J Magn Reson 136:159–168.

23. Halse M, et al. (2004) Centric scan SPRITE magnetic resonance imaging: optimization of SNR, resolution, and relaxation time mapping. *J Magn Reson* 169:102–117.

24. Khrapitchev AA, Newling B, Balcom BJ (2006) Sectoral sampling in centric-scan SPRITE magnetic resonance imaging. J Magn Reson 178:288–96.

25. Romanenko KV, Cano-Barrita PFdJ, Balcom BJ (2009) Cl-35 profiling using centric scan SPRITE with variable flip angle excitation. *J Magn Reson* 198:24–30.

26. Romanenko KV, Balcom BJ (2012) Permeability mapping in naturally heterogeneous sandstone cores by magnetization prepared centric-scan sprite. *AIChE* 58:3916–3926.

27. Romanenko K, et al. (2014) Anisotropic MRI contrast reveals enhanced ionic transport in plastic crystals. *J Am Chem Soc* 136:15638–15645.

28. Romanenko K, Pringle JM, O'Dell LA, Forsyth M (2015) New insights into the thermal behaviour of organic ionic plastic crystals: magnetic resonance imaging of polycrystalline morphology alterations induced by solid-solid phase transitions. *Phys Chem Chem Phys* 17:18991–9000.

29. Adair A, Mastikhin IV, Newling B (2018) Motion-sensitized SPRITE measurements of hydrodynamic cavitation in fast pipe flow. *Magn Reson Imaging* 49:71–77.

30. Callaghan PT (1993) *Principles of Nuclear Magnetic Resonance Microscopy* (Oxford University Press, Oxford).

31. Bernstein MA, King KF, Zhou XJ (2004) *Handbook of MRI Pulse Sequences* (Elsevier Academic Press).

32. Robinson S, Schödl H, Trattnig S (2014) A method for unwrapping highly wrapped multi-echo phase images at very high field: UMPIRE. *Magn Reson Med* 72:80–92.

33. Reichenbach JR, Venkatesan R, Yablonskiy DA, Thompson MR, Lai S, Haacke EM (1997) Theory and application of static field inhomogeneity effects in gradient-echo imaging. *J Magn Reson Imag* 7:266-279.

FIGURE CAPTION

Fig. 1. (A) A timing diagram of the centric-scan SPRITE pulse sequence. (B) Sectoral *k*-space trajectories. The k_X-k_Y plane is divided into 8 sectors. In a 3D acquisition, this scheme is repeated for a number of equally spaced k_Z values. (C) Transverse {*x*-*y*} and longitudinal {*x*-*z*} views of the battery holder with respect to B_0 and B_1 field directions.

Fig. 2. (A) Longitudinal {*y*-*z*} and {*x*-*z*} slices through the 3D FLASH image of the battery holder containing the intact iPhone-5 battery. (B) {*y*-*z*} and {*x*-*z*} slices through the 3D FLASH MF map. The binary mask shows H_2O-containing regions. (C) The regions of MF map in (B) with SNR > 3. FLASH *TE* range: 2.45 - 2.8 ms.

Fig. 3. (A) Longitudinal {*y*-*z*} and {*x*-*z*} slices through the 3D SPRITE image of the battery holder containing the intact iPhone-5 battery, T_P: 0.12 ms. (B) {*y*-*z*} and {*x*-*z*} slices through the 3D MF map reconstructed based on 8 FID points of a single SPRITE scan. The SPRITE *k*-space sampling parameters were $N = 64$, $N_{int} = 64 \times 8$; T_P range: 0.11 - 0.15 ms; ROIs: 53 × 90 mm^2. The binary mask shows H_2O-containing regions. (C) A schematic of the iPhone battery, {*y*-*z*} and {*x*-*z*} views, with current collector and the leads shown in red.

Fig. 4.

Longitudinal slices {*x*-*z*} and {*y*-*z*} through the 3D SPRITE MF maps of the damaged iPhone-5 batteries: (A) A 4 mm hole was punched through the middle of the lower half of the battery and the leads were removed, as indicated on the right. (B) A 16 mm hole was punched through the middle of the lower half of the battery and the top half of the current collector was removed, as indicated on the right. The 3D MF maps were reconstructed based on 8 FID points of a single SPRITE scan. The SPRITE *k*-space sampling parameters were $N = 64$, $N_{int} = 64 \times 8$; T_P range: 0.11 - 0.15 ms; ROIs: 53 × 90 mm^2. The binary mask shows H_2O-containing regions.

Fig. 5. Photographs of the intact (A) and damaged (B) PS batteries. Longitudinal slices {*x*-*z*} through 3D MF maps reconstructed from FLASH (C, D) and SPRITE (E, F) images of the PS batteries. The FLASH *TE* range: 2.45 - 2.8 ms. The SPRITE *k*-space sampling parameters: $N = 37$, $N_{int} = 37 \times 4$; T_P range was 0.1 - 0.33 ms, and the ROI was 41 × 41 mm^2. The space occupied by the battery is indicated with the rectangle.

Figure 6. Histograms of MF perturbation variation ($\delta\Delta B_0$) due to change in SOC of the iPhone-5 battery. The inserts show longitudinal slices $\{x\text{-}z\}$ through 3D MF maps for two states of charge.

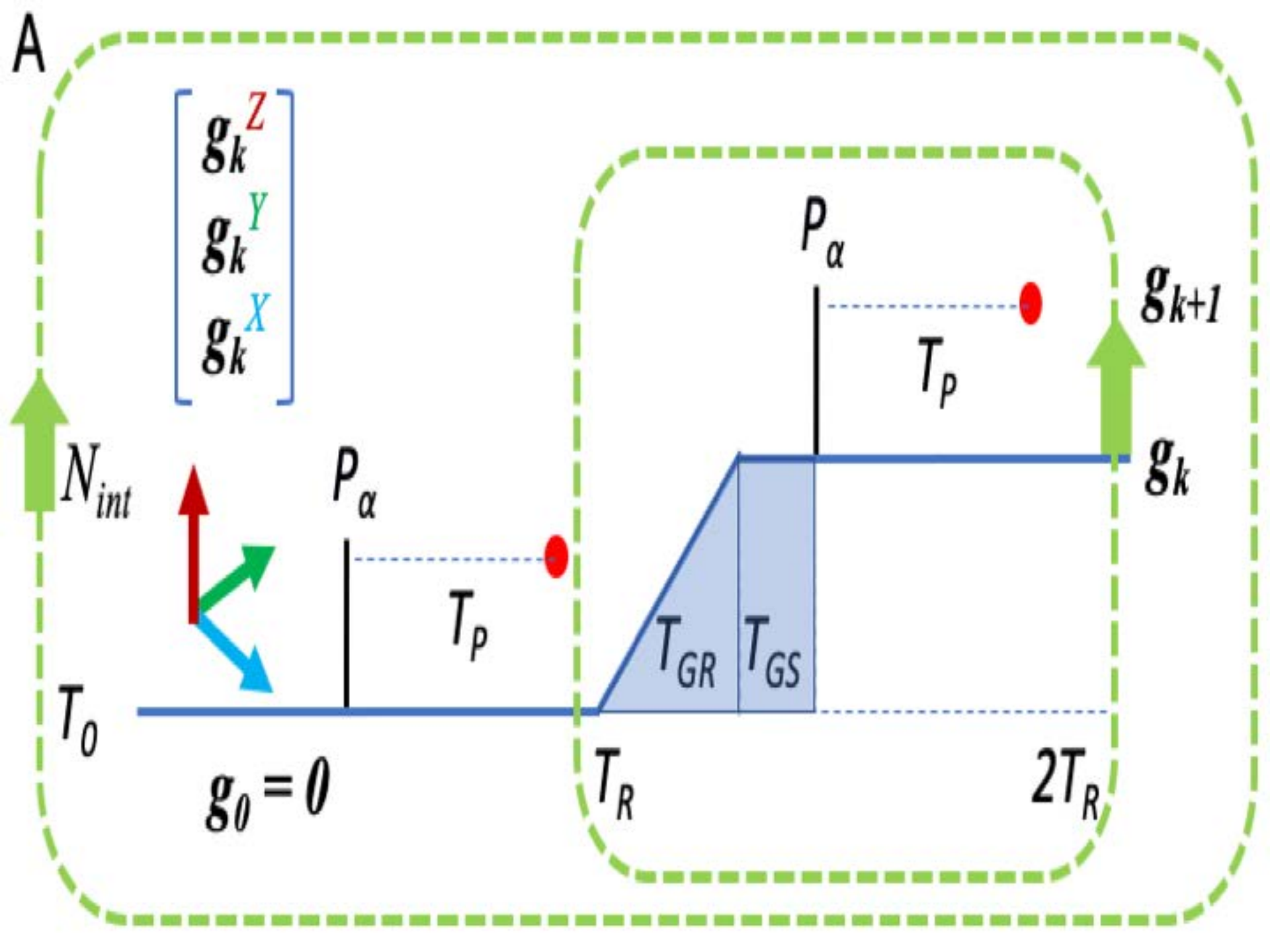
A
g_k^Z
g_k^Y
g_k^X
N_{int}
P_α
T_P
T_O
$g_0 = 0$
P_α
T_P
g_{k+1}
g_k
T_{GR}
T_{GS}
T_R
$2T_R$

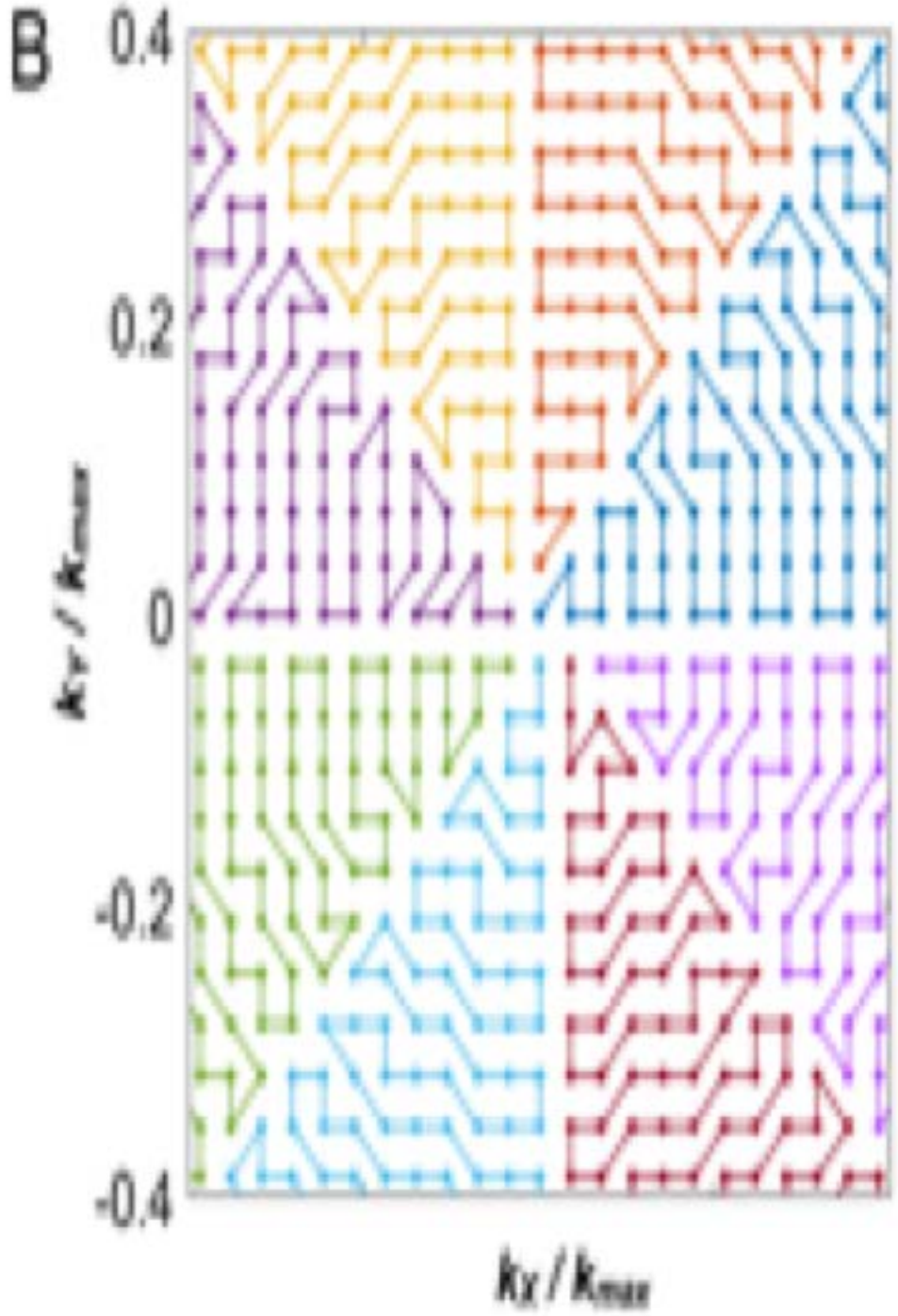
B
0.4
0.2
0
-0.2
-0.4
ky / kmax
kx / kmax

C

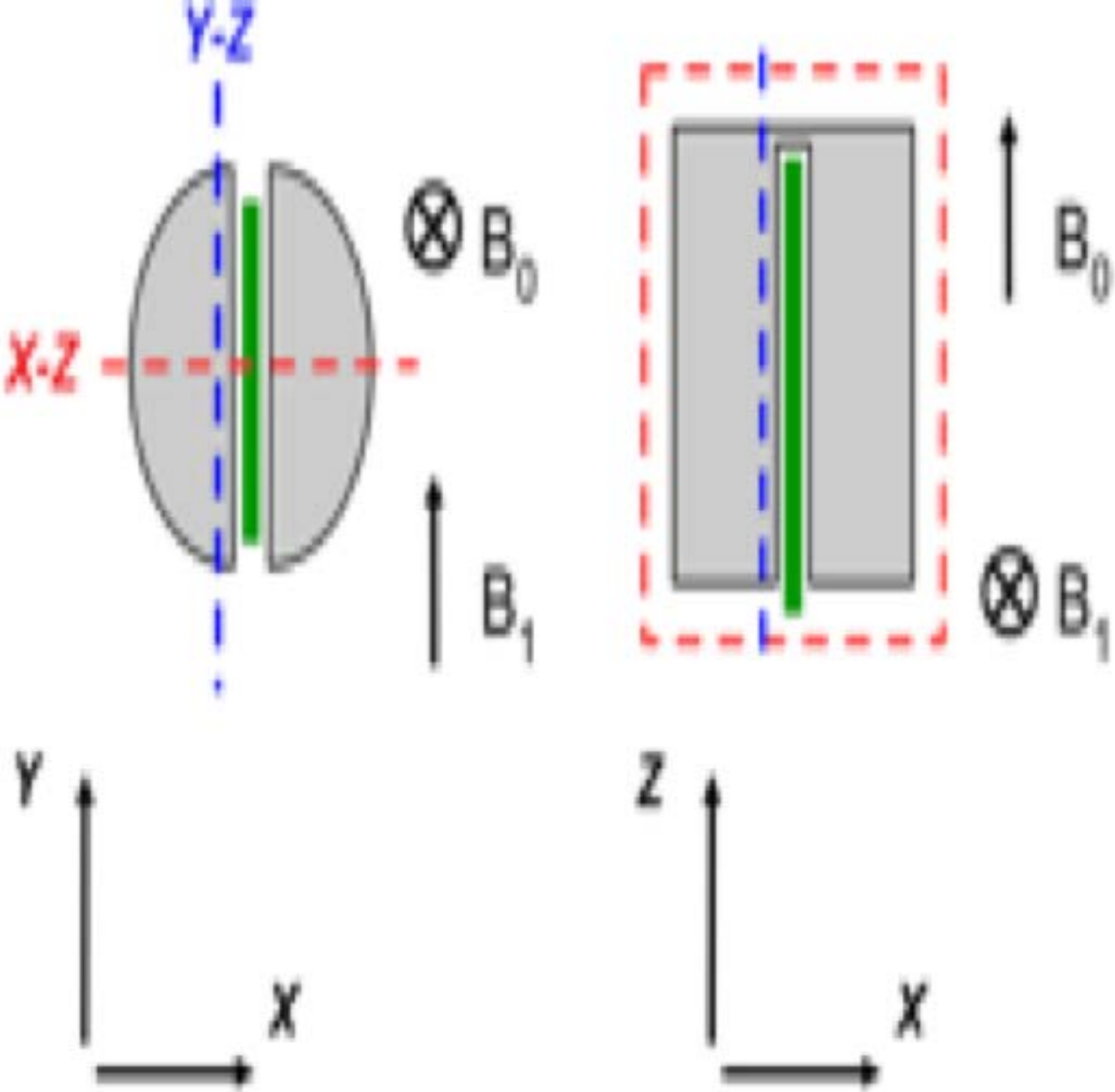

A

Y - Z

1
0.8
0.6
0.4
0.2
0

T_2* weighted density

B

10
8
6
4
2
0
-2
-4
-6
-8
-10

ΔB_0 (ppm)

C

10
8
6
4
2
0
-2
-4
-6
-8
-10

ΔB_0 (ppm)

X - Z

1
0.8
0.6
0.4
0.2
0

T_2* weighted density

10
8
6
4
2
0
-2
-4
-6
-8
-10

ΔB_0 (ppm)

10
8
6
4
2
0
-2
-4
-6
-8
-10

ΔB_0 (ppm)

A

Y - Z

1
0.8
0.6
0.4
0.2
0

T_2* weighted density

B

20
15
10
5
0
-5
-10
-15
-20

ΔB_0 (ppm)

C

X - Z

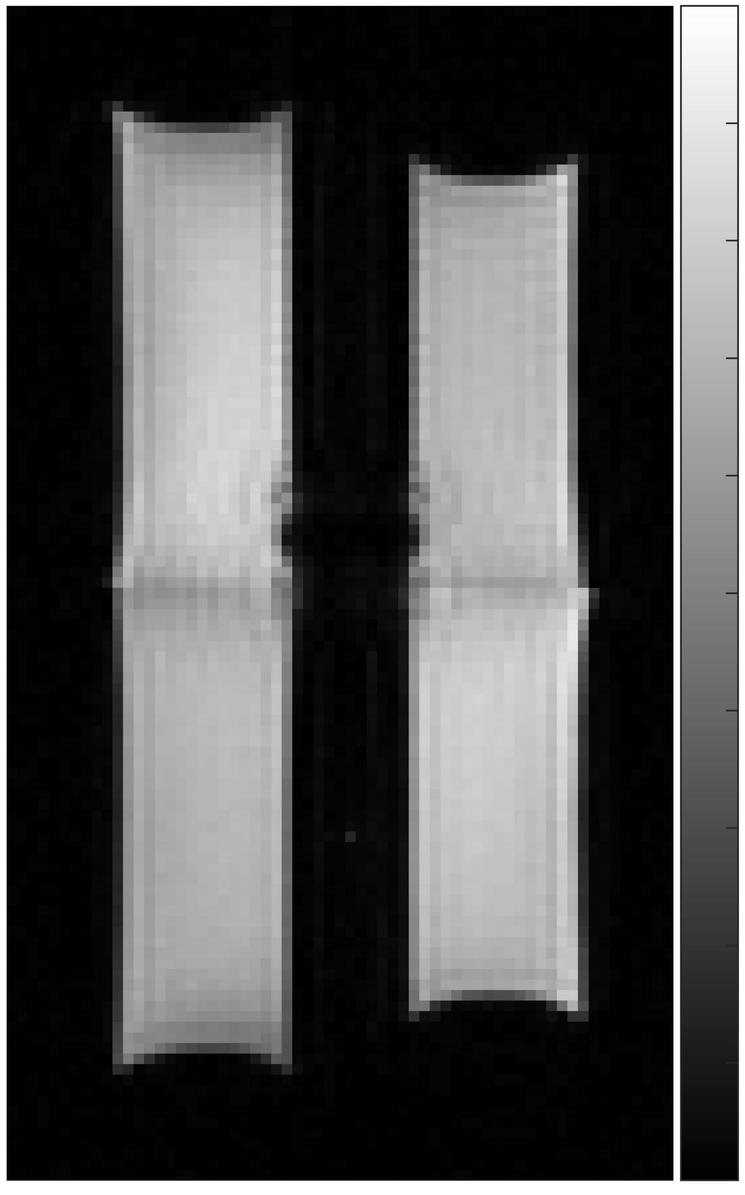

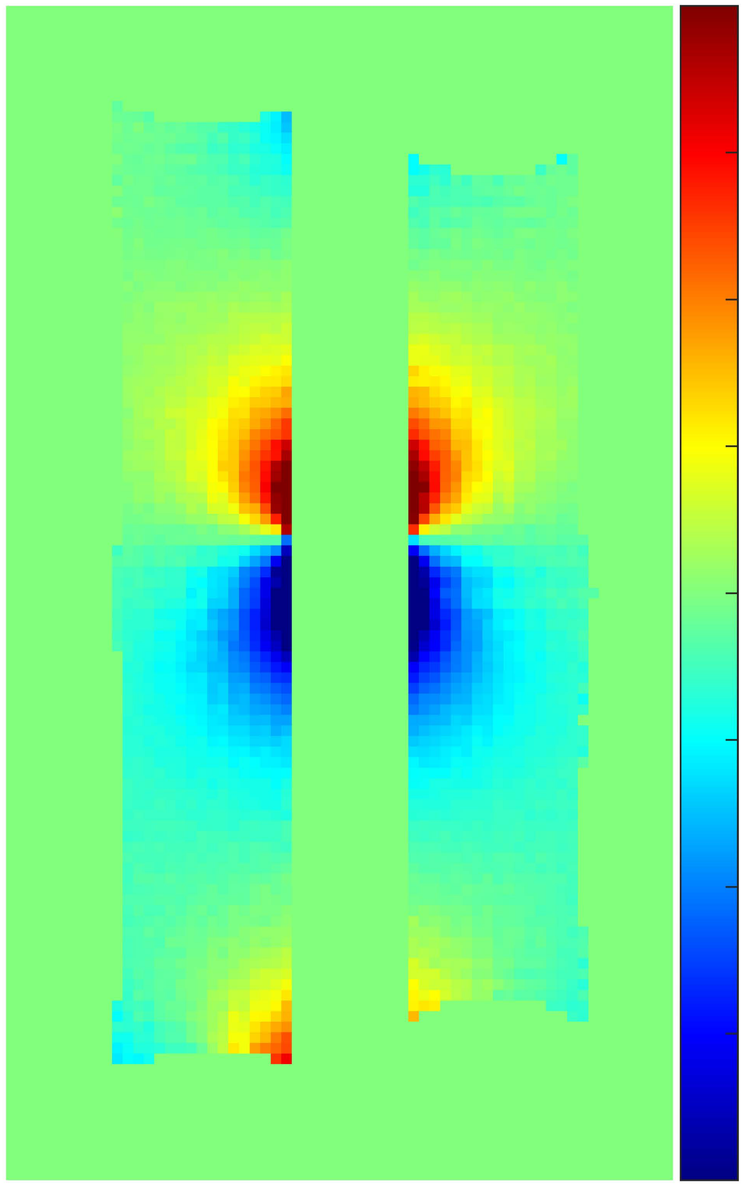

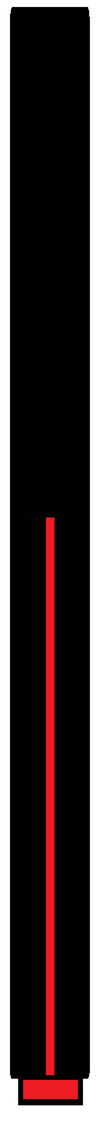

A

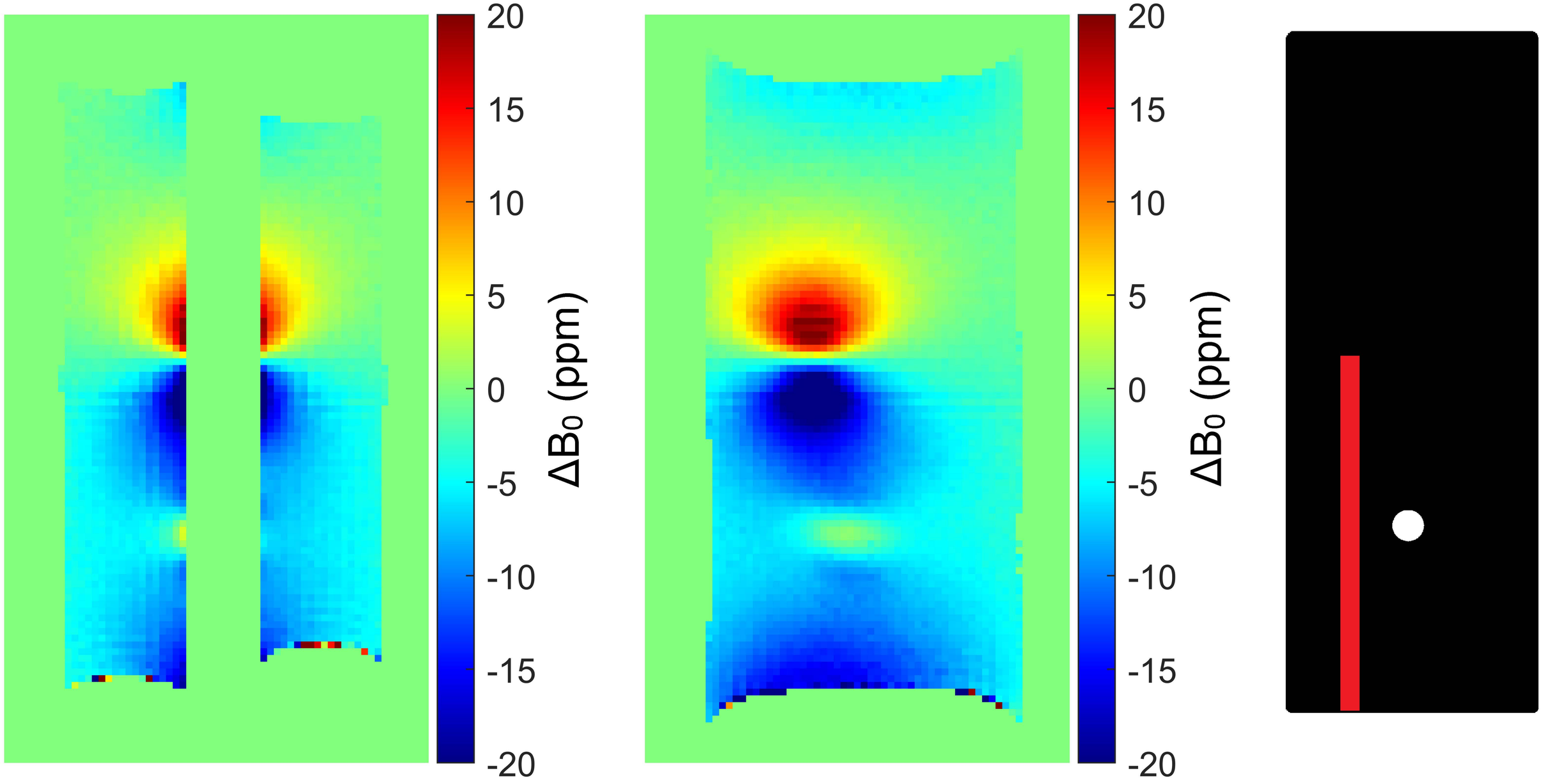
X - Z
Y - Z
Y - Z
20
15
10
5
0
-5
-10
-15
-20
ΔB0 (ppm)
20
15
10
5
0
-5
-10
-15
-20
ΔB0 (ppm)

B

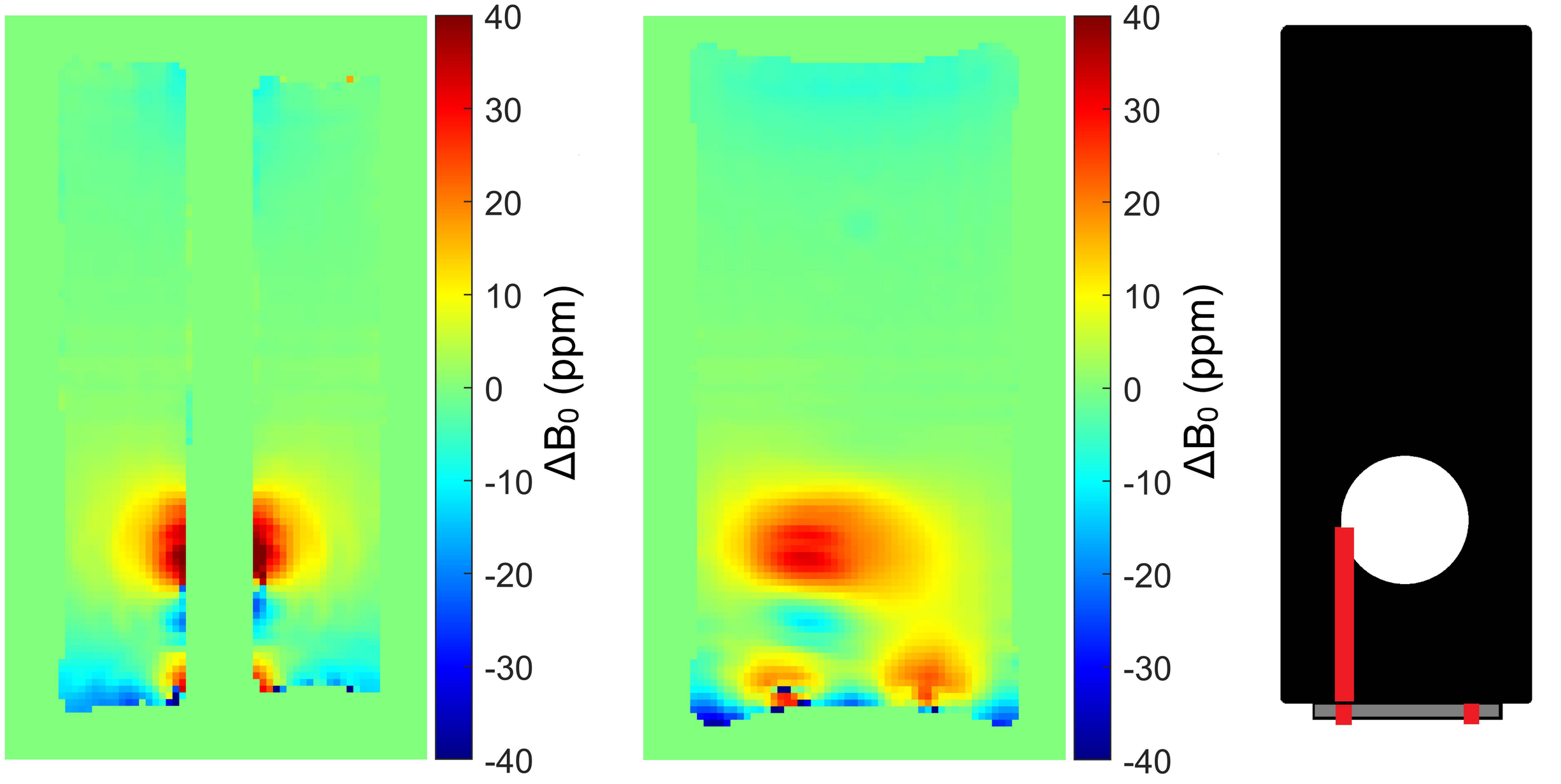
40
30
20
10
0
-10
-20
-30
-40
ΔB0 (ppm)
40
30
20
10
0
-10
-20
-30
-40
ΔB0 (ppm)

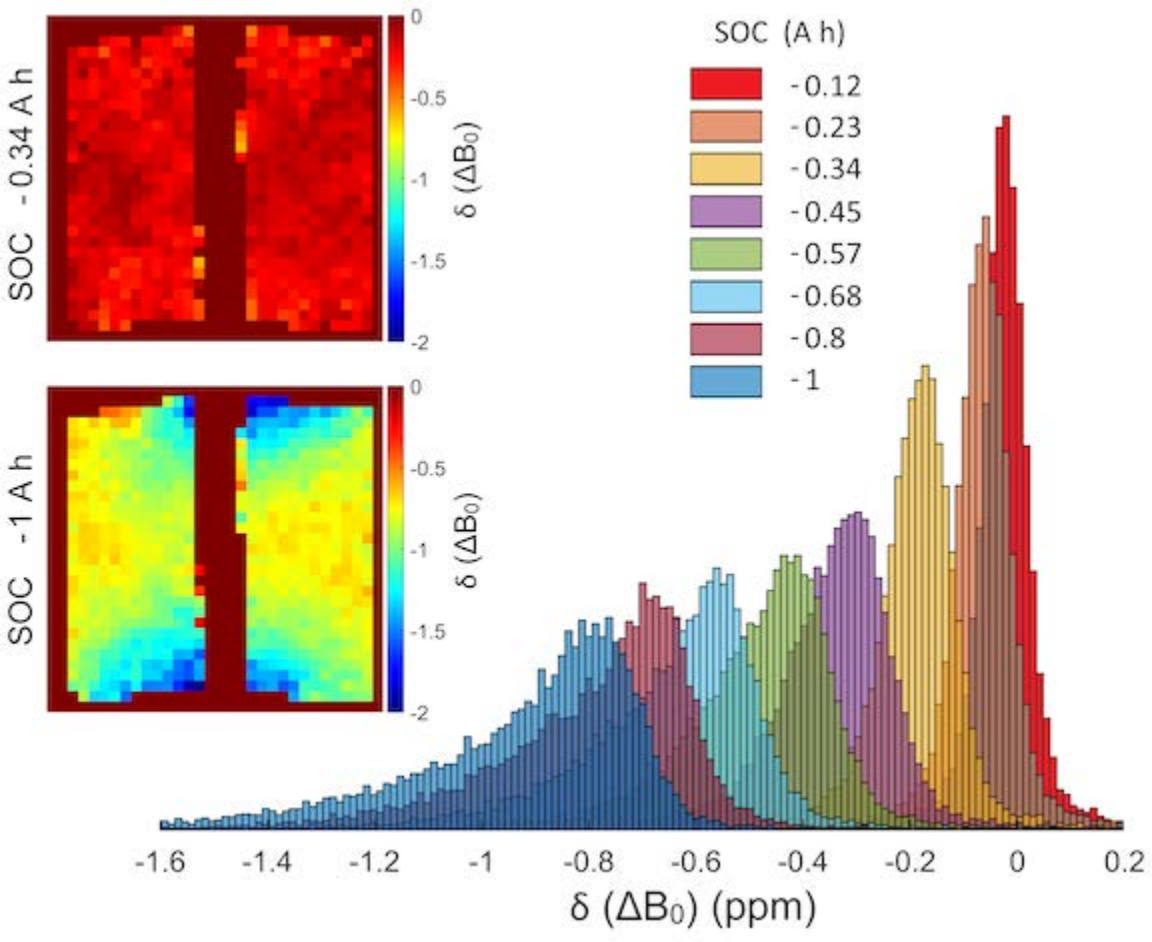
SOC - 0.34 A h
SOC - 1 A h
δ (ΔB0)
0
-0.5
-1
-1.5
-2
SOC (A h)
- 0.12
- 0.23
- 0.34
- 0.45
- 0.57
- 0.68
- 0.8
- 1
-1.6
-1.4
-1.2
-1
-0.8
-0.6
-0.4
-0.2
0
0.2
δ (ΔB0) (ppm)